Hindawi
Advances in Materials Science and Engineering
Volume 2019, Article ID 5105612, 16 pages
https://doi.org/10.1155/2019/5105612

Research Article

Studies on Quasi-Static and Fatigue Crack Propagation Behaviours in Friction Stir Welded Joints Using Peridynamic Theory

Fei Wang, Yu'e Ma, Yanning Guo, and Wei Huang

School of Aeronautics, Northwestern Polytechnical University, Xi'an 710072, China

Correspondence should be addressed to Yu'e Ma; ma.yu.e@nwpu.edu.cn

Received 30 April 2019; Revised 3 August 2019; Accepted 11 October 2019; Published 31 October 2019

Academic Editor: Paolo Ferro

The friction stir welding (FSW) technology has been widely applied in aircraft structures. The heterogeneity of mechanical properties in weld and the hole in structure will lead the crack to turn. Peridynamics (PD) has inherent advantages in calculating crack turning. The peridynamic theory is applied to study the crack turning behaviour of FSW joints in this work. The compact tension (CT) samples with and without a hole are designed. The crack propagation testing under quasistatic and fatigue loads are performed. The peridynamic microplastic model is used and a three-stage fatigue calculation model is developed to simulate the quasistatic fracture and the fatigue crack growth. The results predicted by the peridynamic models are compared with the experimental ones. The effects of welding direction on quasistatic and fatigue crack propagation behaviours are investigated and the effect of hole position on crack path geometry is also studied. It is shown that the crack turning in FSWed CT samples can be captured by the peridynamic microplastic and the three-stage fatigue calculation models. The peridynamic crack growth rates agree with the experimental results. For CT specimen without a hole, the crack turns into the weld zone where the material is softer. The effect of welding direction on crack growth rates is not obvious. For CT sample with a hole, the crack propagation direction has been mainly controlled by the hole location and the welding direction has a slight effect on crack path.

1. Introduction

The increasing need for reductions of weight and production costs in aircraft vehicles has led to reexamination of techniques that have been applied for component manufacturing [1]. In aircraft structural design, a promising solution is to use welded integral structures instead of riveted components. To achieve this goal, the application of the friction stir welding (FSW) has received more and more attention [2–4]. Since FSW has been widely applied in aircraft structure, the crack propagation behaviour is an important problem of FSW structural integrity accessing.

Crack propagation behaviour of FSWs was investigated by experimental and numerical methods [5]. The previous published results indicate that the failure mechanism in the FSWed structure is governed by complicated factors, such as weld material heterogeneity, welding direction, and hole in joints. The weld zone consists of the weld nugget zone (WNZ), the thermomechanically affected zone (TMAZ), and the heat affected zone (HAZ). Due to the material heterogeneity, the fracture toughness in weld is varying with the position. And the weld material exhibited lower tensile properties than the base material (BM). In addition, the welding direction also determines the locations of advancing and retreating sides in TMAZ, so the weld material heterogeneity is affected by welding direction as well. The crack propagation is usually a result of competition between material fracture toughness and crack driving force [6]. The crack paths of FSW joints are not as straight as one normally expected in a mode I testing. The crack turning was observed in CT specimens with a transverse weld [7]. The crack growth behaviour when the crack is in different weld locations was studied in Ref. [8]. FSWed CT specimens with a crack at the middle of weld were analyzed and it can be

found that the crack grew in the middle of the weld and titled into the TMAZ which corresponded to the advancing side. Similarly, the crack path of FSWed CT sample has been observed to deviate away from the center weld line and the nugget region. Then, the crack grew into the TMAZ on the advancing side and propagated in the TMAZ until the specimen failure [9]. The crack derivations in mode I and I/II fracture were also studied, and the heterogeneity of the weld material has a great effect on crack propagation behaviour [10–12]. The effect of a drilled hole on crack trajectory in FSWed single-edge notched tension (SET) specimen was investigated in [13]. The hole position changed the crack trajectory appreciably. Hence, the crack in structure with weld and hole will be deviated.

The deviation of crack usually changes mode I fracture into mixed-mode. Some numerical methods can be applied to simulate crack deviation. According to the ways to model cracks, there are two types of numerical methods: the implicit and the explicit approaches. The implicit approaches do not require cracks to be explicitly modelled, such as the weight function solution [14] and the Trefftz solutions [15–17]. They are suitable for evaluating stress intensity factors (SIFs) of engineering problems but powerless in monitoring of crack paths. The explicit approaches are mainly discussed here, such as the finite element method (FEM), FEM with cohesive zone elements (CZE), the scaled boundary finite element method (SBFEM), the extended finite element method (XFEM), the boundary element method (BEM), the dual boundary element method (DBEM), and the element-free Galerkin method (EFGM). The propagation of cracks in FSW joints has been studied by FEM in [18, 19]. In FEM, the remeshing algorithm is needed. This algorithm is implemented at every crack increment [20]. The time costs are increased by it in calculations. Moreover, an extra crack propagation criterion is requested to predict the crack increment and the kinking angle for every step, such as the maximum tangential stress criterion [21]. The CZE can be introduced in FEM to simulate mixed-mode crack propagation [22]. However, the crack can only propagate between elements. The accuracy of crack trajectory predicted by CZE is not satisfying. The SBFEM is presented to calculate mixed-mode crack propagation in [23]. The remeshing algorithm is still required in SBFEM even though the changes of the global mesh are very small. The crack growth of FSW joints is investigated by XFEM as well [24]. The XFEM permits crack to extend through elements without any remeshing process [25], but the extra computational techniques such as the local enrichment functions, the level set method, and the fracture criterion are still required during analysis. The BEM was also applied to model crack propagation. To solve general crack problem, it is impossible to apply BEM directly in a single region analysis [26]. This disadvantage led to the development of the DBEM [27]. The DBEM incorporated the traction boundary integral equation and the displacement equation. Hence, the mixed-mode crack propagation can be modelled in a single region. The EFGM is a meshless method. It only requires the description of geometry and the data of node. The connectivity data of element are not required [28]. But similar to other methods, an extra fracture criterion to predict the kinking angle and the size of crack extension increment is still demanded in DBEM and EFGM.

To avoid the disadvantages in previous numerical methods, the bond-based peridynamics (BB-PD) was developed by Silling [29]. It unifies the mechanics of discrete particles, discontinuities, and continuous medium. Instead of using the partial derivatives of displacements, the basic peridynamic equation is formulated in an integro-differential form. The interactions of material points are connected via bonds and take place within a horizon. The most significant advantage of peridynamics is the way to model fracture behaviour. In classical continuum mechanics, precrack surfaces are defined as the domain boundaries. The way to introduce a precrack in peridynamics is to remove all the bond connections that cross the precrack surface. Therefore, discontinuities such as cracks and defects can be easily modelled in peridynamics. The extra techniques such as the fracture criterion used in classical continuum mechanics are not needed to simulate damage evolution in peridynamics. The bonds in peridynamics have a critical relative elongation, which can be calculated from the fracture toughness of a specific material. A bond fails when its deformation reaches the critical value. The damage of a material point can be obtained by calculating the fraction of the broken bond number and the initial bond number [30]. The crack propagation can be monitored by the damage evolutions of all points. The peridynamics is relatively simple in numerical implementation and it can accurately predict most fracture behaviours. Peridynamics also has the advantage of meshless method due to the feature of integro-differential equation. Thus, peridynamics has inherent advantages in simulating crack propagation.

Peridynamics has been applied to investigate fracture behaviour of solid structure. Peridynamic fracture model for brittle materials was reviewed by Bobaru and Zhang [31]. The plastic fracture modelled by peridynamics was verified [32, 33]. A microplastic model for the bond-based peridynamics has been implemented in ABAQUS to simulate penetration damage under impact [34] and crack mouth open displacement under quasistatic load [35]. A material degradation fatigue model based on peridynamics was proposed by Oterkus and Guven [36]. This approach can be used to predict the damage accumulation for the growth phase of fatigue cracking. Silling and Askari [37] proposed a fatigue model that each bond was characterized by a damage variable which was called remaining life. And it can be applied to both the crack initiation and growth phases. Zhang et al. [38] used this remaining life model to study the fatigue cracking in homogeneous and composite materials. Jung and Seok [39, 40] developed this fatigue model to calculate the fatigue crack growth of functionally graded materials (FGMs) and the mixed-mode fatigue crack propagation of homogeneous materials. According to the Paris-Erdogan relation, Hu and Madenci [41] proposed a peridynamic fatigue model to calculate the residual stiffness, the residual strength, and the damage for fiber reinforced composites.

However, numerical studies on crack propagation of FSW joints under quasistatic and fatigue load using peridynamic model have not been published. The goal of this paper is to investigate and discuss the effects of welding direction and hole position on crack path geometry in FSWed CT samples.

2. Peridynamic Theory

2.1. Microplastic Model. Because peridynamics is formulated by using integrations instead of derivatives of displacements, the mathematical inconsistencies in the classical continuum mechanics are avoided in peridynamics. The basic peridynamic equation can be written as [42]

$$\rho(\mathbf{x})\ddot{\mathbf{u}}(\mathbf{x},t) = \int_{H_{\mathbf{x}}} \mathbf{f}\left(\mathbf{x}',\mathbf{x},t\right)\mathrm{d}V_{\mathbf{x}'} + \mathbf{b}(\mathbf{x},t), \tag{1}$$

where $\mathbf{f}$ is the pairwise bond force density function, see Figure 1. Its form can be determined by deformation and material properties through constitutive model. Constant δ can be called the horizon size. The circle area with a radius size of δ can be called the family or the horizon of a node, denoted $H_{\mathbf{x}}$. $\mathbf{x}$ is the center node. The family of a node is constructed by all the particles within its circle area. If the distance of a bond is longer than horizon size, the interaction between these two nodes is vanished. ρ is the material density. $\ddot{\mathbf{u}}$ is the acceleration. $\mathbf{b}$ is the body force density.

The pairwise force function $\mathbf{f}$ in bond-based model can be given as [43]

$$\mathbf{f}(\boldsymbol{\xi},\boldsymbol{\eta},t) = f(\boldsymbol{\xi},\boldsymbol{\eta},t)\mathbf{M}, \tag{2}$$

where

$$\boldsymbol{\eta} = \mathbf{u}\left(\mathbf{x}',t\right) - \mathbf{u}(\mathbf{x},t),\ \boldsymbol{\xi} = \mathbf{x}' - \mathbf{x}, \tag{3}$$

in which $\mathbf{u}(\mathbf{x}, t)$ is the displacement and f is the scalar bond force. $\mathbf{M}$ is a direction vector of a deformed bond:

$$\mathbf{M} = \frac{\boldsymbol{\eta} + \boldsymbol{\xi}}{|\boldsymbol{\eta} + \boldsymbol{\xi}|}. \tag{4}$$

To facilitate constitutive models, the bond strain s can be defined as

$$s = \frac{|\boldsymbol{\eta} + \boldsymbol{\xi}| - |\boldsymbol{\xi}|}{|\boldsymbol{\xi}|}. \tag{5}$$

For microplastic material, f can be taken as [34]

$$f(\boldsymbol{\xi},\boldsymbol{\eta},t) = \mu c\left(s - s_p\right). \tag{6}$$

The elastic-perfectly plastic constitute law under tension load at bond level is illustrated in Figure 2.

The micromodulus c can be obtained by matching strain energy density in peridynamics and its value in classical continuum mechanics. For plane stress, the definition of c is:

$$c = \frac{12k}{\pi h \delta^3}, \tag{7}$$

where h is the thickness. k is the bulk modulus. Its definition is

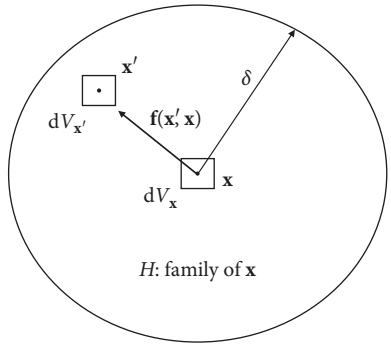

Figure 1: Peridynamic horizon of node $\mathbf{x}$.

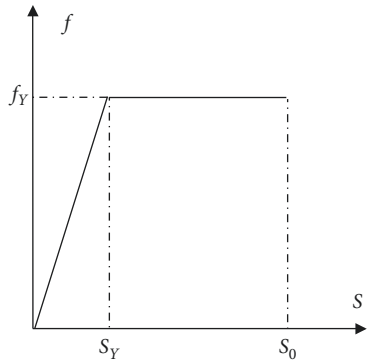

Figure 2: Microplastic material model.

$$k = \frac{E}{2(1-\nu)}, \tag{8}$$

where E is the elastic modulus. ν is Poisson's ratio, and it is limited to 1/3 for plane stress. $s_p = s_p(t)$ is the plastic bond strain history and it can be defined as

$$\frac{\mathrm{d}}{\mathrm{d}t}s_p = \begin{cases} 0, & \text{if } \left|s - s_p\right| < s_Y, \\ \dfrac{\mathrm{d}}{\mathrm{d}t}s, & \text{otherwise,} \end{cases} \qquad \left(s_p(0) = 0\right), \tag{9}$$

where s_Y is the bond yield strain. The relation of yield stress and bond yield strain can be obtained by integrating the peridynamic force density within the horizon. The definition of bond yield strain for plane stress is [43]

$$s_Y = \frac{12\sigma_Y}{c\pi h \delta^3}, \tag{10}$$

where σ_Y can be taken as the material yield strength [35].

The bond failure can be introduced by the function μ. The plastic fracture of a bond can be determined by

$$\mu(\boldsymbol{\xi},t) = \begin{cases} 1, & s < s_0, \\ 0, & \text{otherwise,} \end{cases} \tag{11}$$

where s_0 is the critical relative elongation of a bond for failure. The strain at ultimate strength is used for the critical relative elongation [34].

The damage of a node is defined as the fraction of the broken bond number and the total initial bond number:

$$\varphi(\mathbf{x},t) = 1 - \frac{\int_{H_\mathbf{x}} \mu(\boldsymbol{\xi},t)\mathrm{d}V_{\mathbf{x}'}}{\int_{H_\mathbf{x}} \mathrm{d}V_{\mathbf{x}'}}. \tag{12}$$

2.2. Fatigue Model. The fatigue fracture for a bond is determined by

$$\mu(\boldsymbol{\xi},t) = \begin{cases} 1, & s < s_c \text{ and } 0 < \lambda \le 1, \\ 0, & \text{otherwise}, \end{cases} \tag{13}$$

where s_c is the critical relative elongation of elastic materials. The relationship between it and the fracture energy G_{IC} was derived by Silling [29]. For plane stress, it can be expressed as

$$s_c = \sqrt{\frac{4\pi G_{\mathrm{IC}}}{9E\delta}}, \tag{14}$$

where $G_{\mathrm{IC}} = {K_{\mathrm{IC}}}^2/E$. Variable λ is the remaining life of a bond. It evolves over fatigue cyclic time. The initial value of remaining life for each bond is unity. The relation of λ and cycle number N for fatigue crack growth phase can be written as [37, 38]

$$\frac{\mathrm{d}\lambda}{\mathrm{d}N} = -A_2\varepsilon^{m_2}, \tag{15}$$

where ε is the cyclic bond strain range and for linear elastic materials it is defined as

$$\varepsilon = \left|s^+ - s^-\right| = \left|(1-R)s^+\right|. \tag{16}$$

The s^+ and s^- are the maximum and the minimum bond strains in one cycle. Load ratio $R = s^-/s^+$. Hence, only the response under the maximal loading is required during calculating. A_2 and m_2 are positive parameters. m_2 is obtained from Paris law data. The Paris law is well known as

$$\frac{\mathrm{d}a}{\mathrm{d}N} = C\Delta K^M, \tag{17}$$

where C and M are Paris material constants. Variable a is the crack length and N is the cycle number. Silling and Askari [37] derived the relationship between the stress intensity factor and the core bond strain. Then, the relation of the core bond strain and the peridynamic fatigue crack growth rates can be expressed as

$$\frac{\mathrm{d}a}{\mathrm{d}N} = \beta A_2 \varepsilon_c^{m_2}, \tag{18}$$

where β is a proportional constant, which is only dependent on δ and m_2. m_2 is equivalent to M. To obtain A_2, a calculation test is performed with an arbitrary A_2 value. This value is called A_i. The predicted crack growth rates can be expressed as

$$\left(\frac{\mathrm{d}a}{\mathrm{d}N}\right)_i = \beta A_i \varepsilon_c^{m_2}. \tag{19}$$

According to equations (18) and (19), the following relation is derived:

$$A_2 = A_i G, G = \frac{\mathrm{d}a/\mathrm{d}N}{(\mathrm{d}a/\mathrm{d}N)_i}. \tag{20}$$

The $\mathrm{d}a/\mathrm{d}N$ in equation (20) is the real crack growth rates, which the result of Paris law is used in this work. G can be regarded as correction factor.

2.3. Numerical Implementations. Even if the basic equation is in dynamic form, peridynamics can still be used to calculate static problem by applying extra computational techniques, such as FEM coupled method [34], the Adaptive Dynamic Relaxation (ADR) technique [44], the energy minimization method [45], and the artificial damping method [46]. The ADR is chosen because its algorithm is simple and reliable. The midpoint quadrature scheme is used to calculate the peridynamic integration in basic equation. The volume correction [31] is also involved. The energy method [47] is applied to implement surface correction.

The fatigue calculation process of our program includes three stages. Stage 1 is the testing stage. The arbitrary value A_i is given and the correction factor G_1 is calculated. Stage 2 is called the calibration stage. The crack growth rates can be obtained by using $A_2 = A_i G_1$ and the correction factor G_2 is obtained. Stage 3 is called the correction stage. The results of crack growth rates are obtained by $A_2 = A_i G_1 G_2$. The basic quasistatic and fatigue fracture numerical procedure is presented in Figures 3(a) and 3(b) m is the total particle number of a discretized structure. n is the horizon node number for one particle.

3. Experiments and Calculations

3.1. Specimen Configurations. 8 mm thick 2024 aluminium alloy (AA) plates are welded. The FSW joint compact tension (CT) specimens (samples 1 and 3) and the CT specimen with a hole (sample 2) are designed according to ASTM standard [48] ($W = 100$ mm). The geometries of the specimens are illustrated in Figure 4. The width of the weld is 20 mm. The A side and the R side mean the advancing side and the retreating side of the weld. The crack propagation experiments for FSW joint CT specimens are carried out. Samples 1 and 2 are tested under quasistatic load and sample 3 is tested under fatigue load.

3.2. Peridynamic Parameters for FSWs. The FSW joints can be divided into different regions. The material properties of FSWs can be simplified as a function of vertical coordinate. According to the research of Tzamtzis [49], the material properties of weld can be determined by the stress-strain curves of different weld zones. The small differences are observed in HAZ and BM. Thus, the HAZ is treated as the same as BM. Based on the tests of Tzamtzis [49], the material ratio of weld material to base metal is used to characterize the heterogeneity of weld material. The material properties of 2024 AA are shown in Table 1 [49]. The elastic and plastic

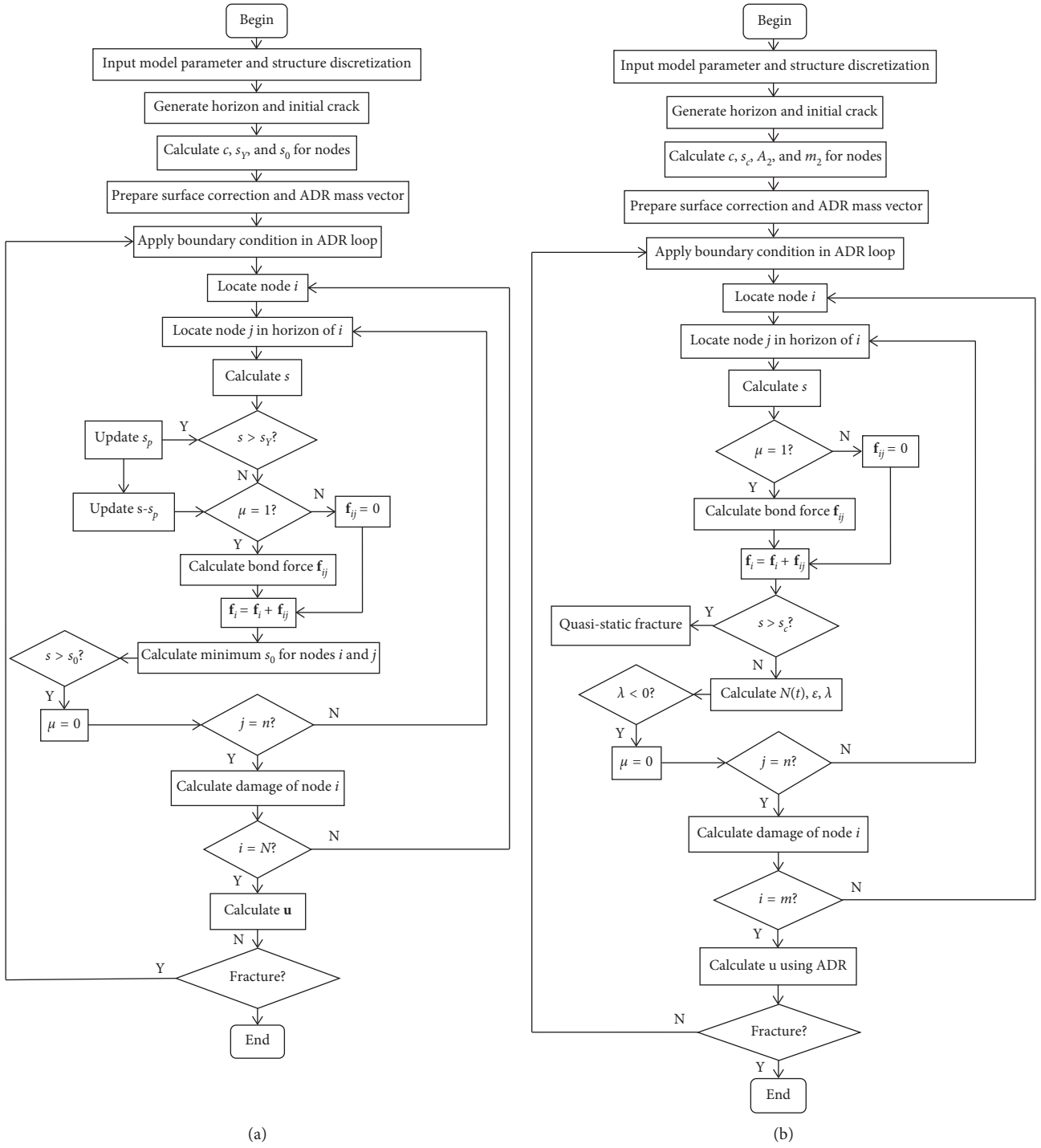

Figure 3: Peridynamic numerical implementations. (a) Quasistatic fracture algorithm. (b) Fatigue fracture algorithm.

material ratios of different weld zones to BM are illustrated in Figure 5(a). The fatigue parameters of FSW joint obtained from experiment are specified. The material ratios of fatigue parameters for different weld zones are shown in Figures 5(b) and 5(c).

All parameters, such as the micromodulus c, the strain for brittle failure s_c, the bond yield strain s_Y, the strain for plastic fracture s_0, the fatigue parameters m_2 and A_2 for a bond that crosses different regions, can be evaluated by the average model [39, 50].

3.3. Experimental and Calculation Results. A 100 kN servo-hydraulic machine is used to perform quasistatic crack propagation tests at room temperature with a constant displacement rate 1.0 mm/min. The ultimate loads of

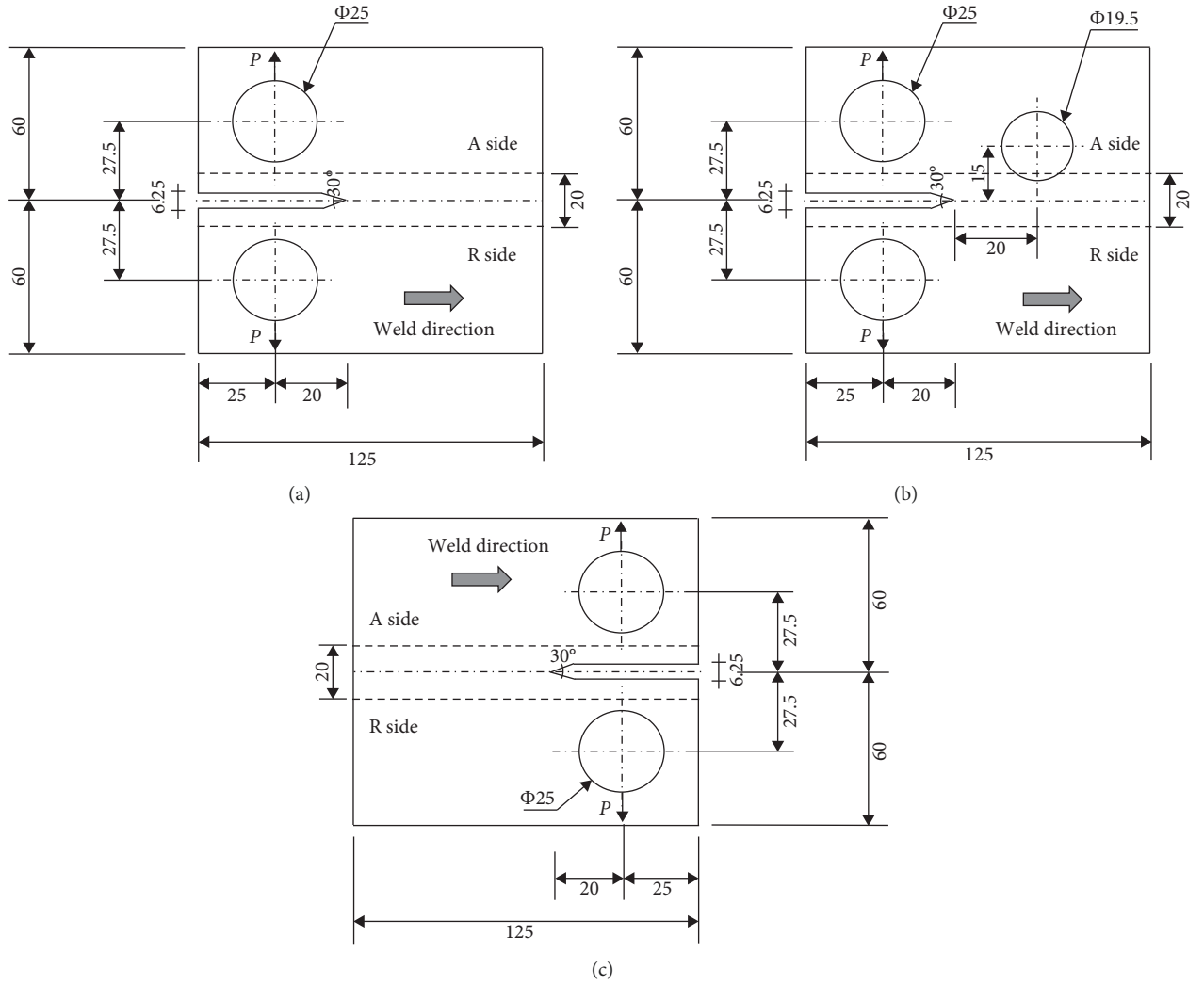

Figure 4: The configurations of FSWed samples. (a) CT specimen (sample 1). (b) CT specimen with a hole (sample 2). (c) CT specimen for fatigue (sample 3).

Table 1: Material properties of base metal.

Material	E (GPa)	ν	K_{IC} (MPa·m$^{1/2}$)	σ_Y (MPa)	s_0
2024 AA	73.1	0.33	60	327	0.185

samples 1 and 2 are 47.8 kN and 39.5 kN, respectively. The measured crack paths are shown in Figures 6(a) and 6(c).

The FSWed CT samples are machined from the welded 2024 AA plates. The samples before testing have been performed posttreatments to release residual stresses. Furthermore, cracks in the samples are parallel to the weld. In this case, the effect of residual stress can be ignored [51]. Any differences in crack path and growth rate observed can be ascribed to material fracture toughness and load effects [9]. Therefore, the residual stresses are neglected in the peridynamic calculations.

The horizon size $\delta = 3.015\Delta\mathbf{x}$ is selected as commonly suggested for simulations [52]. The node spacing $\Delta\mathbf{x} = 0.001$ m is used here. The displacement rate load used in experiment is converted to the force load. The mechanical responses with these two loading methods are the same. The peridynamic force density that is equivalent to force P is applied on the nodes with the maximal absolute value of vertical coordinate on the boundaries of two pin holes [38]. The ADR technique is employed and the time step of ADR procedure is 1.0 s. The 3.50 GHz Intel Xeon CPU and the 8GB RAM are used to implement calculations.

The ultimate loads are selected as the force loads for samples 1 and 2. The crack path results predicted by the peridynamic microplastic model are, respectively, shown in Figures 6(b) and 6(d). The CPU times of the calculations are 219.9 s and 396.7 s.

In Figure 6(a), it can be found that the crack in sample 1 firstly propagates to the advancing side of the weld with a kinking angle. Then, the crack grows straight along the upper edge of weld nugget. The same crack turning phenomenon can be found in the peridynamic numerical result that is given in Figure 6(b).

In Figure 6(c), the crack in sample 2 firstly deviates into the advancing side of the weld and then tilts into the hole.

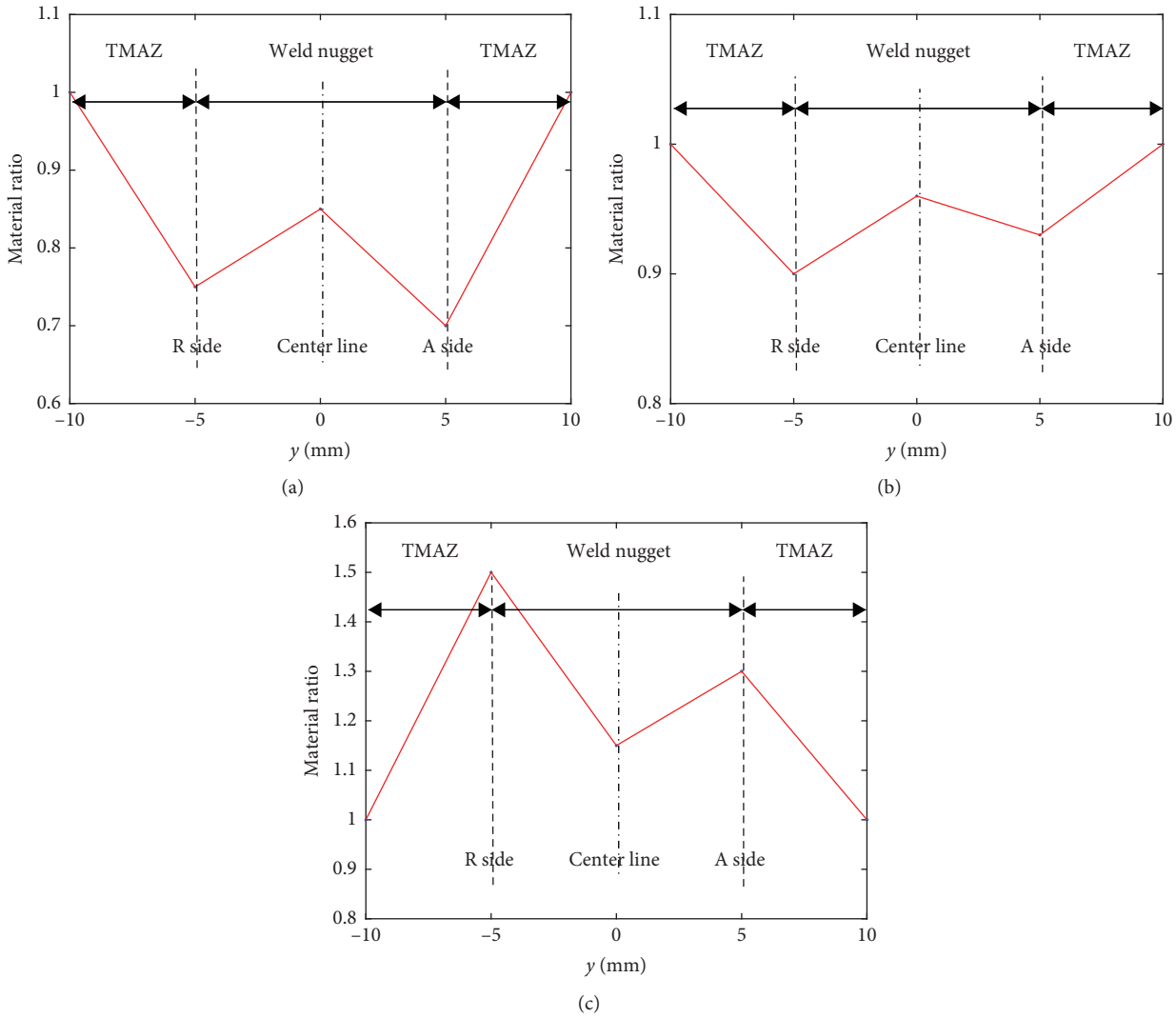

Figure 5: Material ratios of weld zones to base metal. (a) c, s_c, s_Y and s_0, (b) m_2, (c) A_2.

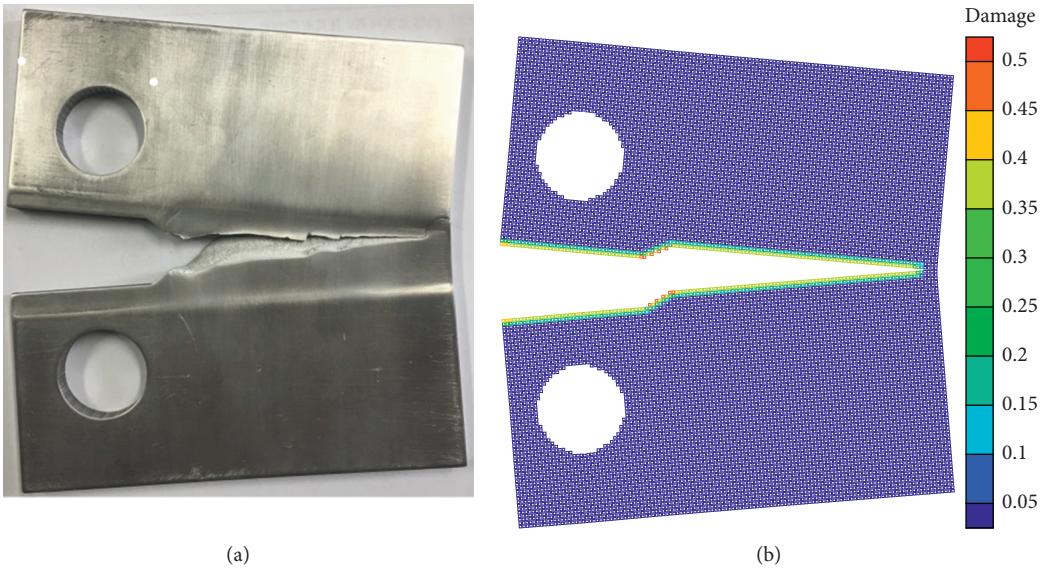

Figure 6: Continued.

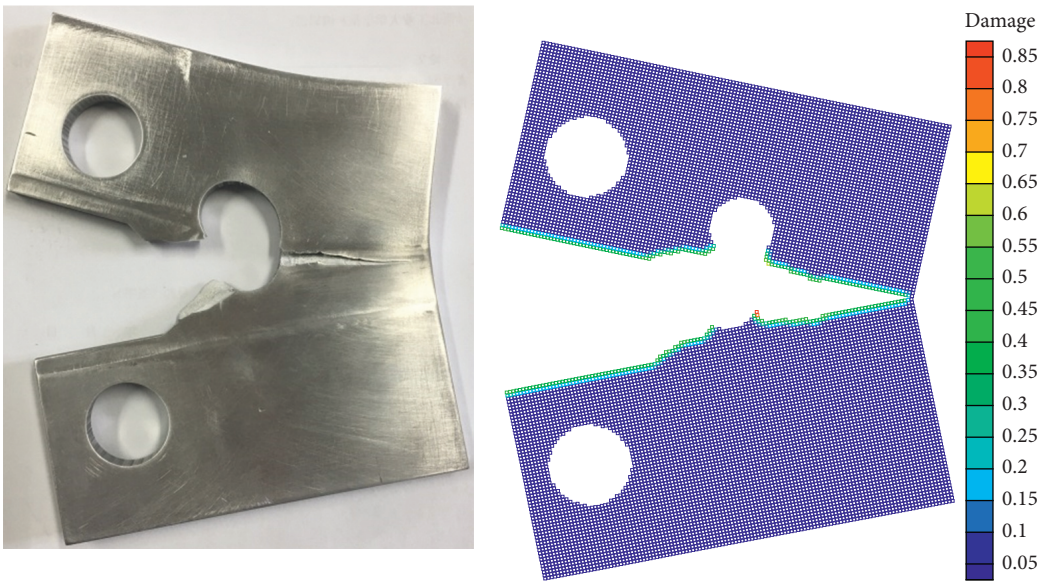

Figure 6: Quasistatic crack path comparison. (a) Experimental crack path of sample 1. (b) Peridynamic crack path of sample 1. (c) Experimental crack path of sample 2. (d) Peridynamic crack path of sample 2.

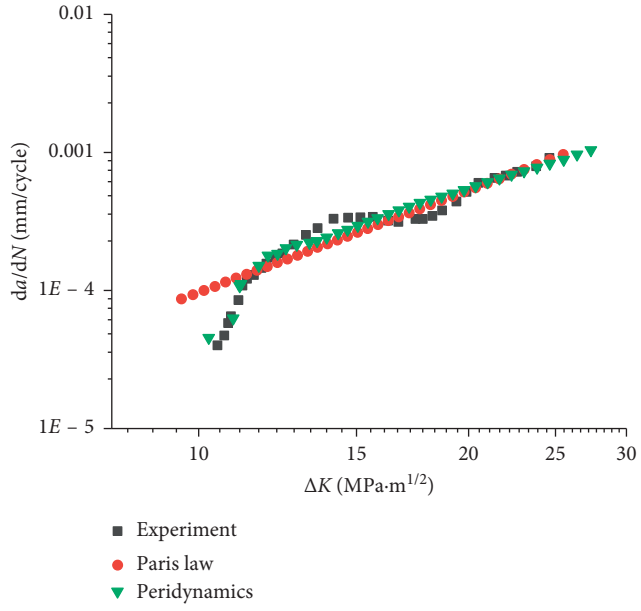

Figure 7: Fatigue crack growth rates of sample 3.

Due to the bottom boundary of the hole is in the weld, a new crack initiation was emerged at the right side of the hole, where is the interface of HAZ and BM. Then, the crack propagates to the weld nugget zone and grows along the upper edge of the weld nugget. In Figure 6(d), the crack derivation observed during testing is also captured by peridynamics. The location and the direction of the new crack at the hole agree with the experimental results.

A 26 kN servo-hydraulic machine is used to perform fatigue crack growth test with a constant amplitude loading. The maximal load is 6.2 kN. The load ratio $R = 0.1$ and the frequency is 20 Hz. Loading amplitude $\Delta P = 5.58$ kN. The stress intensity factor range ΔK is calculated according to the ASTM experimental standard [48]. The Paris parameters of FSWs obtained from experiment are $M = 2.455$ and $C = 3.396e - 7$. To reduce the peridynamic calculation cost, a linear function $N(t) = 20t$ is used to map the fictitious simulation time t with current loading cycle N.

Crack growth rates of experiment and peridynamic results of sample 3 are given in Figure 7. The CPU time of the

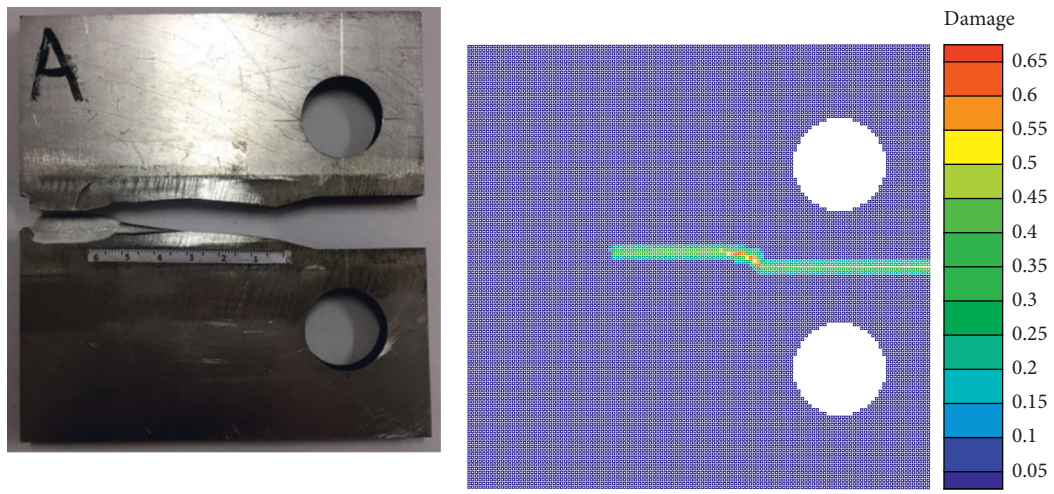

Figure 8: Fatigue crack path comparison. (a) Experimental result of sample 3. (b) Peridynamic result of sample 3.

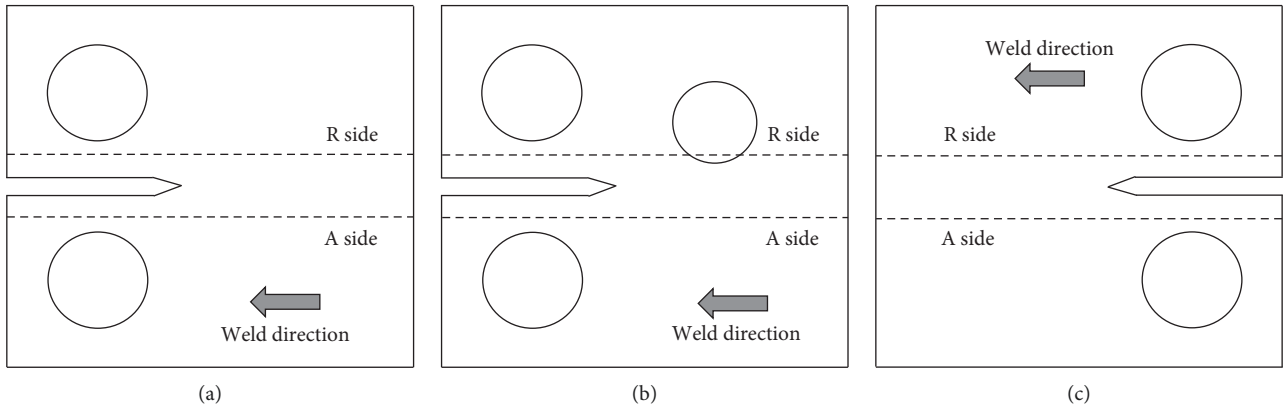

Figure 9: FSWed samples with welding direction heading to left. (a) Sample 4. (b) Sample 5. (c) Sample 6.

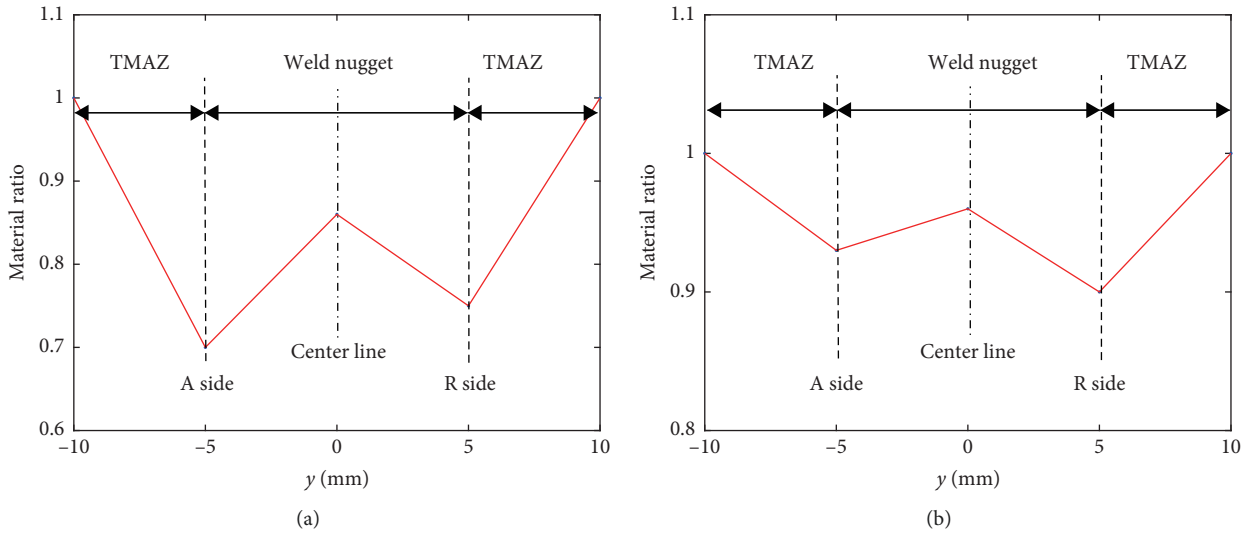

Figure 10: Continued.

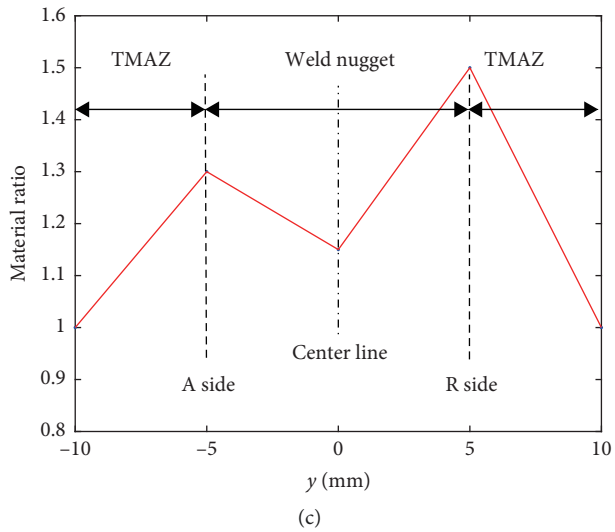

(c)

Figure 10: Material ratios of specimens with welding direction heading to left. (a) c, s_c, s_Y and s_0, (b) m_2, and (c) A_2.

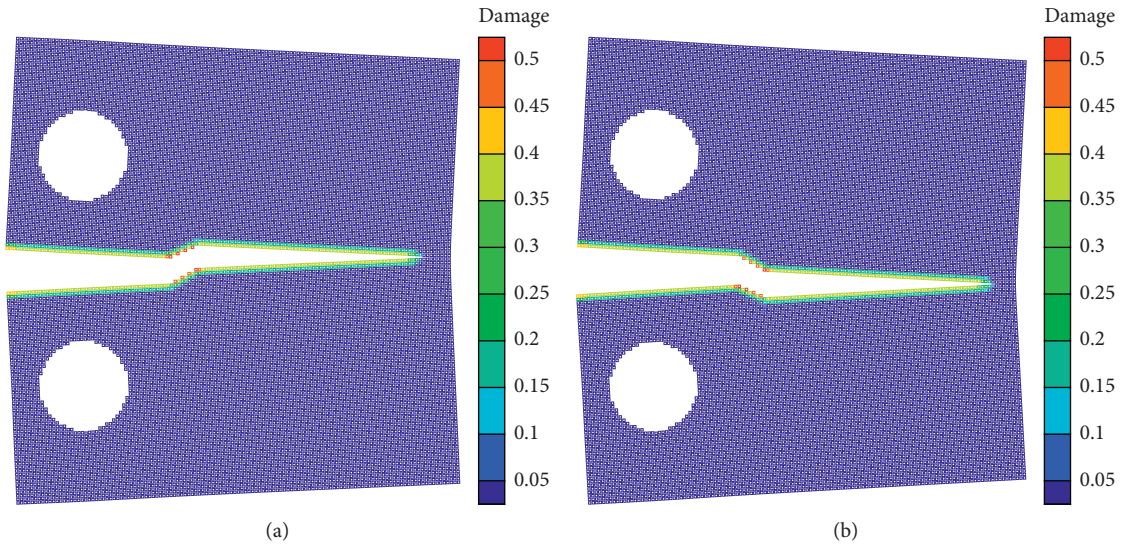

(a) (b)

Figure 11: Quasistatic rack paths for (a) sample 1 and (b) sample 4.

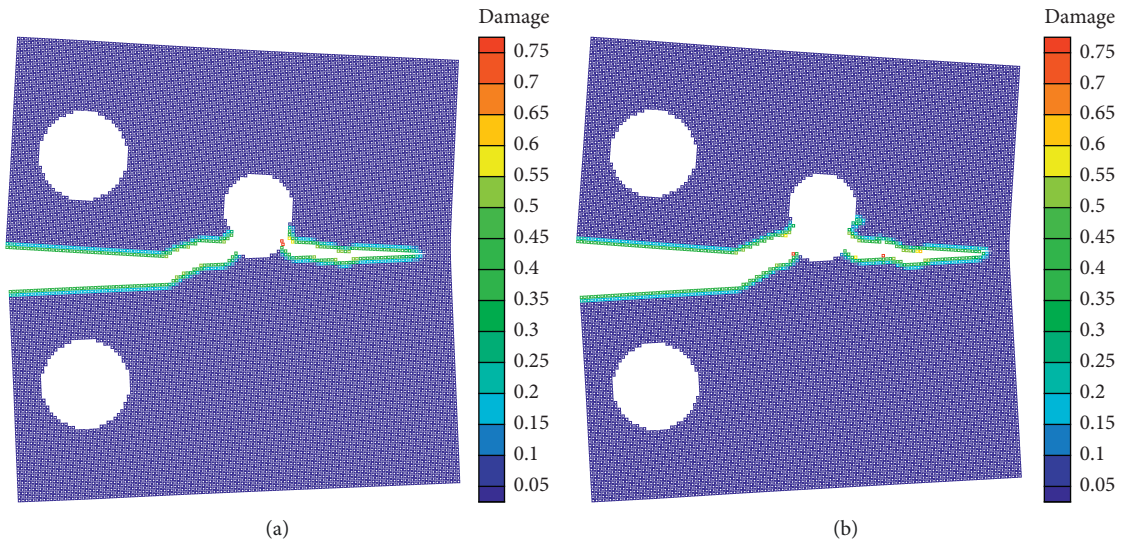

(a) (b)

Figure 12: Quasistatic rack paths for (a) sample 2 and (b) sample 5.

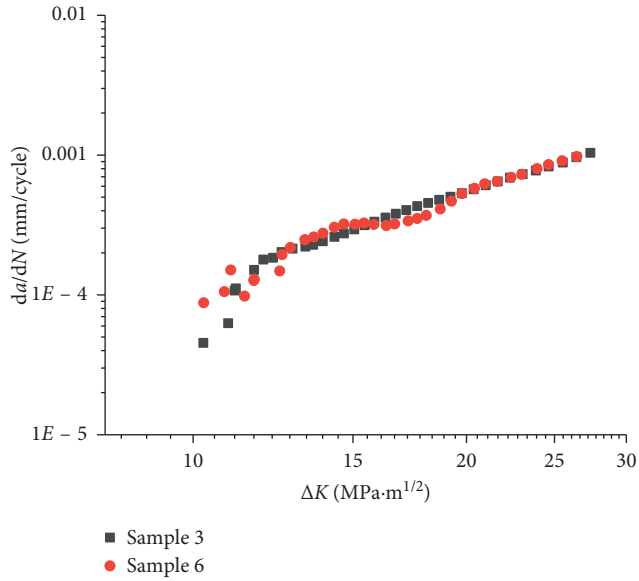

Figure 13: Crack growth rates for samples 3 and 6.

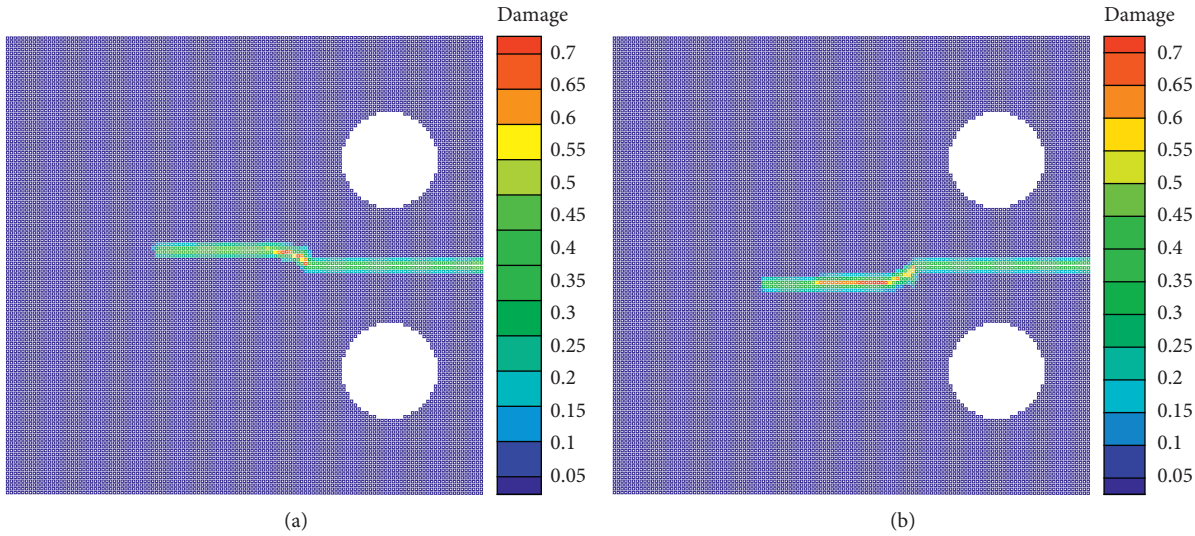

Figure 14: Fatigue crack paths for (a) sample 3 and (b) sample 6.

peridynamic calculation is 4313.5 s. The result of Paris law based on the parameters of M and C is shown as well. The crack growth rates predicted by peridynamics at $\Delta K < 12\,\text{MPa}\cdot\text{m}^{1/2}$ are smaller than the Paris law results, but they are similar to the experimental ones. At $\Delta K > 12\,\text{MPa}\cdot\text{m}^{1/2}$, the crack growth rates predicted by peridynamics agree with the experimental and the Paris law results.

The experimental and the predicted crack paths of sample 3 are, respectively, shown in Figures 8(a) and 8(b). In Figure 8(a), it can be found that the crack firstly propagates to the advancing side with a kinking angle. Then, the crack grows straight along the upper edge of the weld nugget. After the crack length is longer than 60 mm, the crack propagates very quickly. The crack turning is also found in the predicted result in Figure 8(b). The peridynamic fatigue cracking model can capture the crack turning of the FSWed sample.

4. Numerical Results and Discussions

4.1. The Effect of Welding Direction on Crack Path. The CT specimens with welding direction that heading to right and their weld material ratios are shown in Figure 4 (samples 1, 2, and 3). The CT specimens with welding direction heading to left are shown in Figure 9 (samples 4, 5, and 6). The different welding direction leads to a different location of the advancing and the retreating sides. Their material ratios of different weld zones are shown in Figure 10.

The CT specimens without and with a hole under quasistatic load for two welding directions are calculated. The peridynamic modelling parameters and the loads are applied as the same as the samples in experiments. The crack paths when the crack tip reaches the horizontal location around 60 mm are shown in Figures 11 and 12. The coordinate origin is at the geometry center of CT sample.

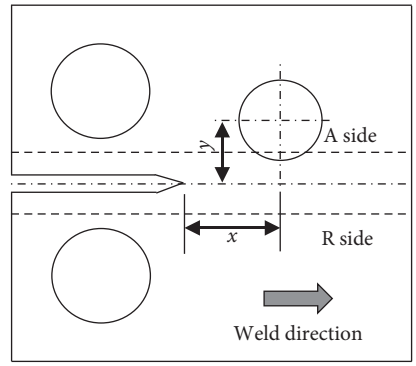

Figure 15: Hole position.

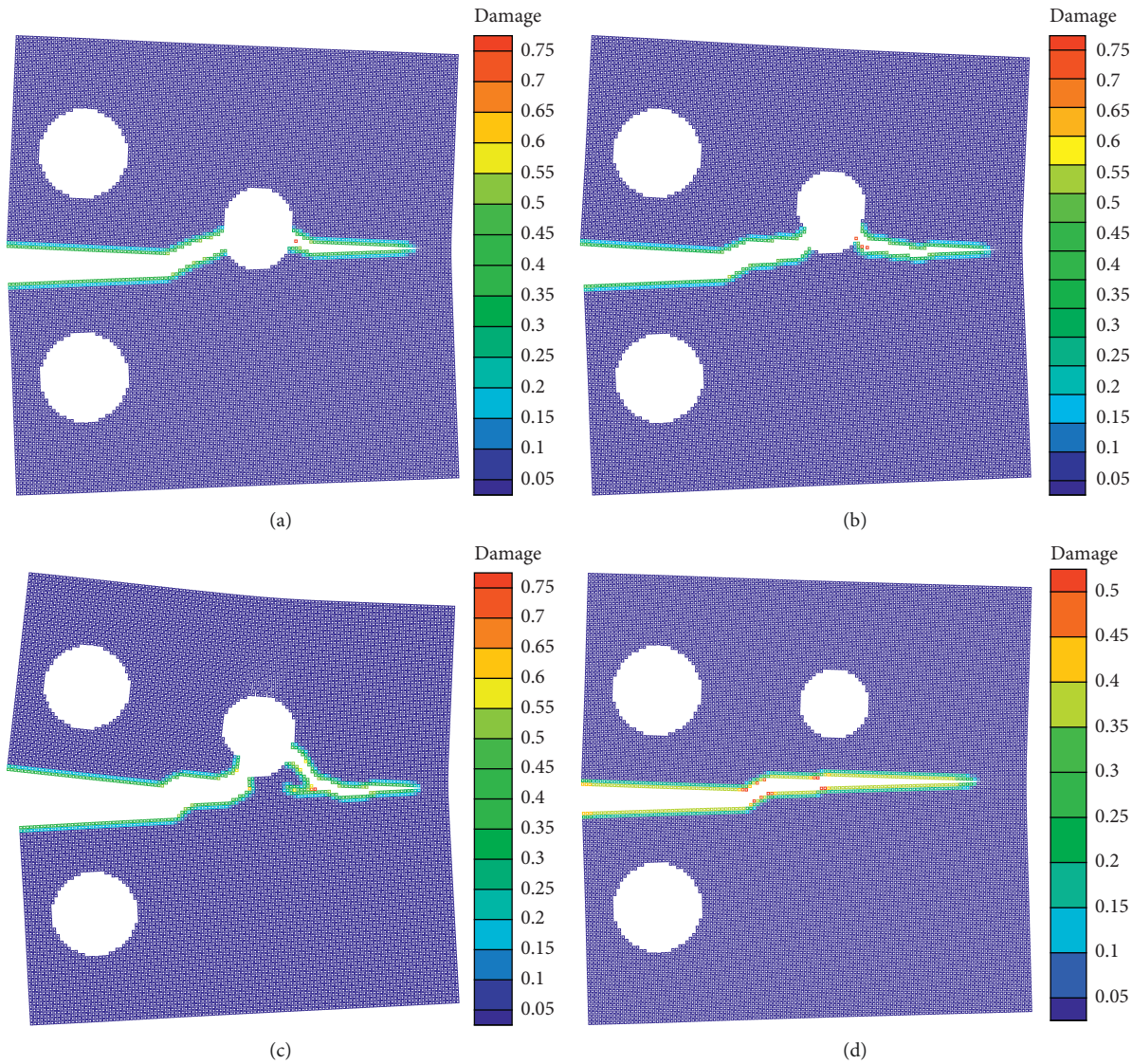

Figure 16: Crack paths with different hole vertical positions when $x = 25$ mm and (a) $y = 10$ mm, (b) $y = 15$ mm, (c) $y = 20$ mm, and (d) $y = 25$ mm.

In Figure 11(a), the crack path of sample 1 is mentioned as before. However, in Figure 11(b), the crack is observed to deviate away from the weld nugget into the TMAZ on the advancing side where is beneath the weld line, and then propagates straight in the TMAZ until the specimen failure. The difference between samples 1 and 4 is the welding

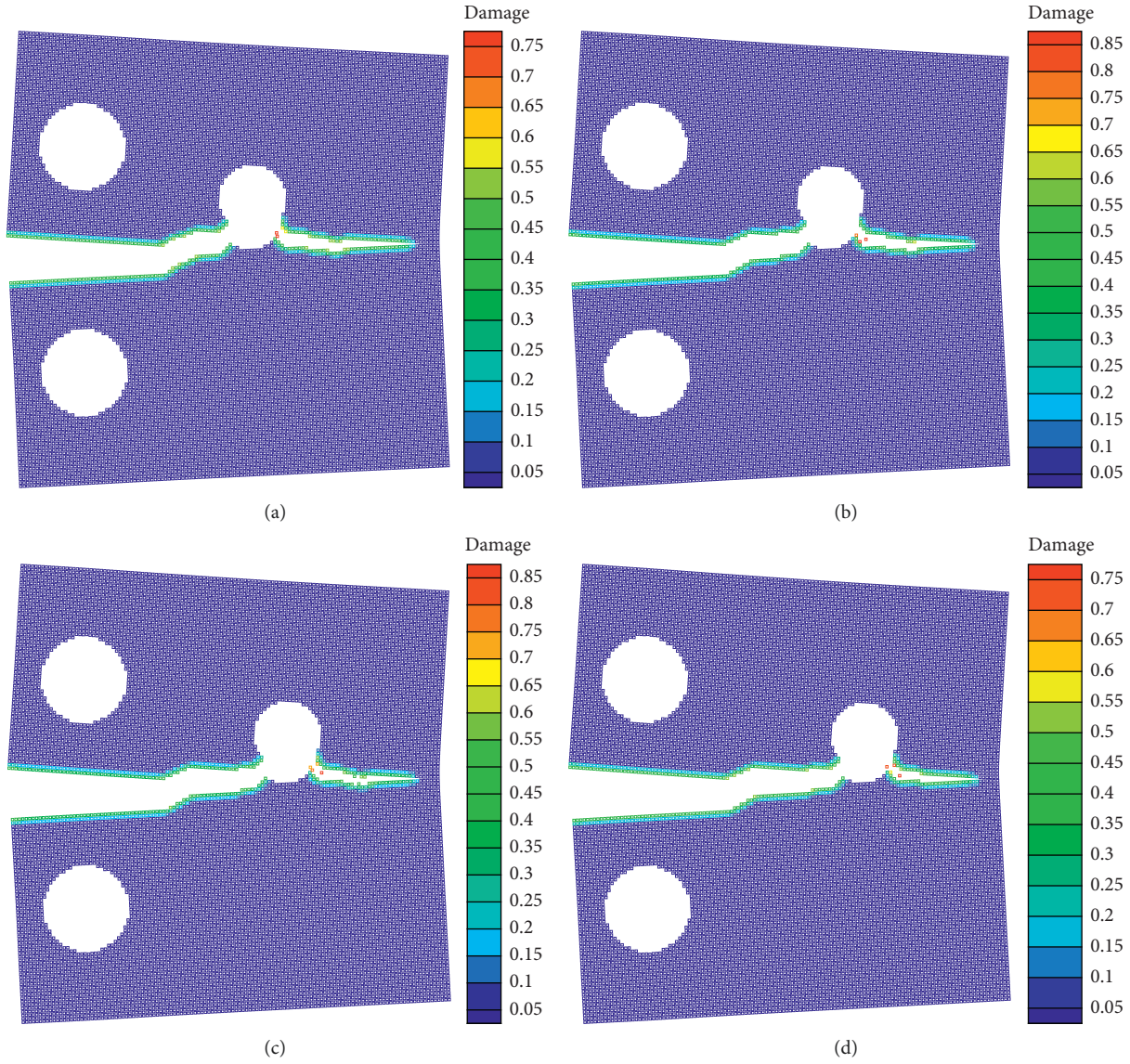

FIGURE 17: Crack paths with different hole horizontal positions when $y = 15$ mm and (a) $x = 25$ mm, (b) $x = 30$ mm, (c) $x = 35$ mm, and (d) $x = 40$ mm.

direction that determines the material ratio distribution (see Figures 5 and 10). It can be found that the cracks firstly propagate to the advancing side because the material in advancing side is more compliant compared with the retreating side material.

As shown in Figure 12(a), the crack path is similar to that in Figure 6(d). The crack firstly grows into the advancing side, then propagates along the weld nugget upper edge, and turns into the hole. There is a short distance in the crack path along the upper edge of the weld nugget. The crack in sample 5 (see Figure 12(b)) grows into the hole directly and it propagates to the retreating side owing to the effect of the hole. The crack growth direction has been mainly controlled by the location of the hole. Compared with the effect of the hole, the effect of welding direction on crack path is slight. For both welding direction cases, after the precrack propagates into the hole, a new crack initiates at the right side of the hole and then this crack propagates into the weld nugget. The effect of welding direction is still not obvious.

The fatigue crack propagations of two welding direction cases are also calculated. The crack growth rates and the crack paths of samples 3 and 6 are shown in Figures 13 and 14.

In Figure 13, when $\Delta K < 12$ MPa·m$^{1/2}$, the crack growth rates of sample 3 are slower than that of sample 6. At $\Delta K > 12$ MPa·m$^{1/2}$, the crack growth rates of sample 6 appear small oscillations. The crack growth rates of two samples are basically similar. The welding direction has a slight effect on fatigue crack growth rates. As shown in Figure 14, the cracks also propagate to the advancing side.

4.2. The Effect of Hole Position on Crack Path. The crack propagation paths in CT samples with different hole positions are calculated. The hole position of the CT specimen is

shown in Figure 15. The horizontal and the vertical locations for the center of the hole are expressed by x and y, respectively.

The crack paths with different vertical hole location y values are shown in Figure 16, and the horizontal location of $x = 25$ mm. When $y = 10$ mm (see Figure 16(a)), the crack directly grows into the hole with a kinking angle. In cases of $y = 15$ mm (see Figure 16(b)) and $y = 20$ mm (see Figure 16(c)), the cracks propagate away from the weld line, grow straight along the upper edge of the weld nugget, and then turn into the TMAZ and the hole. In Figure 16(c), the crack length growing straight along the upper edge of the weld nugget is longer than that in Figures 16(b) and 16(a). With the increasing of the vertical location, the force driving crack into the hole is weaker. Therefore, when $y = 25$ mm (see Figure 16(d)), the crack grows pass the hole which demonstrates that the effect of the hole on crack propagation is very slight.

In Figure 16(c), the relative deformation of the crack root is more obvious than other cases. After the precrack grew into the hole, a new crack emerged at the right side of the hole. However, with the increasing of the hole vertical location, the distance of the new initiating crack to the weld line is longer. Correspondingly, more energy and deformation for driving the crack growing back into the weld nugget are needed. Thus, more deformation and damage are found in Figure 16(c). It can also be validated that the hole can be used to arrest the crack.

The effect of the horizontal location x on crack path is shown in Figure 17. The vertical location $y = 15$ mm. For all cases, the cracks start to grow into the upper edge of weld nugget and propagate along this upper edge then turn into the hole. The horizontal location only affects the crack length in the edge of weld nugget.

5. Conclusions

(1) The crack turning in FSWed sample can be captured by the peridynamic microplastic and the three-stage fatigue calculation model.

(2) The crack growth rates predicted by peridynamics at $\Delta K < 12\,\text{MPa}\cdot\text{m}^{1/2}$ are smaller than the Paris law results, but they are similar to the experimental ones. At $\Delta K > 12\,\text{MPa}\cdot\text{m}^{1/2}$, the crack growth rates predicted by peridynamics agree with the experimental and the Paris law results.

(3) For CT specimen without a hole, the crack firstly turns into the advancing side and then propagates straight along the edge of weld nugget. Cracks turn into the weld zone where the material is softer. The crack growth rates of specimens with two welding directions are similar.

(4) For CT specimen with a hole, the crack firstly grows into the hole. The crack growth direction has been mainly controlled by the hole location. The welding direction has a slight effect on crack path in this case. With the increasing of the hole vertical location, the distance of the new emerging crack to the weld line is longer. The horizontal location of the hole only affects the crack propagating length in the thermomechanically affected zone.

Data Availability

The data used to support the findings of this study are available from the corresponding author upon request.

Conflicts of Interest

The authors declare no conflicts of interest.

Acknowledgments

The authors are grateful for the financial support from the National Natural Science Foundation of China (Grant no. 11572250).

References

[1] W. M. Thomas and E. D. Nicholas, "Friction stir welding for the transportation industries," *Materials & Design*, vol. 18, no. 4–6, pp. 269–273, 1997.

[2] R. Talwar, D. Bolser, R. Lederich, and J. Bauman, "Friction stir welding of airframe structures," in *Proceedings of the Second International Symposium on Friction Stir Welding*, Gothenburg, Sweden, June 2000.

[3] D. Lohwasser, "Welding of airframes by friction stir welding," in *Proceedings of the Third International Symposium on Friction Stir Welding*, TWI, Kobe, Japan, June 2000.

[4] H. Matt, "An emerging joining technology lets manufacturers rethink how products fit together," *Mechanical Engineering*, vol. 12, pp. 1–6, 2003.

[5] X. He, F. Gu, and A. Ball, "A review of numerical analysis of friction stir welding," *Progress in Materials Science*, vol. 65, no. 10, pp. 1–66, 2014.

[6] U. Zerbst, R. A. Ainsworth, H. T. Beier et al., "Review on fracture and crack propagation in weldments-a fracture mechanics perspective," *Engineering Fracture Mechanics*, vol. 132, pp. 200–276, 2014.

[7] G. Pouget and A. P. Reynolds, "Residual stress and microstructure effects on fatigue crack growth in AA2050 friction stir welds," *International Journal of Fatigue*, vol. 30, no. 3, pp. 463–472, 2008.

[8] P. M. G. P. Moreira, A. M. P. de Jesus, A. S. Ribeiro, and P. M. S. T. de Castro, "Fatigue crack growth in friction stir welds of 6082-T6 and 6061-T6 aluminium alloys: a comparison," *Theoretical and Applied Fracture Mechanics*, vol. 50, no. 2, pp. 81–91, 2008.

[9] Y. E. Ma, P. Staron, T. Fischer, and P. E. Irving, "Size effects on residual stress and fatigue crack growth in friction stir welded 2195-T8 aluminium-part I: experiments," *International Journal of Fatigue*, vol. 33, no. 11, pp. 1417–1425, 2011.

[10] M. A. Sutton, A. P. Reynolds, B. Yang, and R. Taylor, "Mode I fracture and microstructure for 2024-T3 friction stir welds," *Materials Science and Engineering A*, vol. 354, no. 1-2, pp. 6–16, 2003.

[11] M. A. Sutton, A. P. Reynolds, B. Yang, and R. Taylor, "Mixed mode I/II fracture of 2024-T3 friction stir welds," *Engineering Fracture Mechanics*, vol. 70, no. 15, pp. 2215–2234, 2003.

[12] M. A. Sutton, A. P. Reynolds, J. Yan, B. Yang, and N. Yuan, "Microstructure and mixed mode I/II fracture of AA2524-

T351 base material and friction stir welds," *Engineering Fracture Mechanics*, vol. 73, no. 4, pp. 391–407, 2006.

[13] Y. E. Ma, B. Q. Liu, and Z. Q. Zhao, "Crack paths in a friction stir-welded pad-up for fuselage applications," *Journal of Aircraft*, vol. 50, no. 3, pp. 879–885, 2013.

[14] T. Fett and D. Munz, *Stress Intensity Factors and Weight Functions*, Computational Mechanics Publications, Boston, MA, USA, 1997.

[15] D. Peng, R. Jones, and T. Constable, "Tools and methods for addressing the durability of rolling stock," *Engineering Failure Analysis*, vol. 34, pp. 278–289, 2013.

[16] R. Jones, D. Peng, R. K. Singh Raman, P. Huang, D. Tamboli, and N. Matthews, "On the growth of fatigue cracks from corrosion pits and manufacturing defects under variable amplitude loading," *JOM*, vol. 67, no. 6, pp. 1385–1391, 2015.

[17] R. Jones, "Fatigue crack growth and damage tolerance," *Fatigue & Fracture of Engineering Materials & Structures*, vol. 37, no. 5, pp. 463–483, 2014.

[18] A. F. Golestaneh and A. Ali, "Application of numerical method to investigation of fatigue crack behavior through friction stir welding," *Journal of Failure Analysis and Prevention*, vol. 9, no. 2, pp. 147–158, 2009.

[19] A. F. Golestaneh, A. Ali, S. Voon Wong, F. Mustapha, and M. Zadeh, "Computational investigation of crack behavior in friction stir welding," *Simulation*, vol. 85, no. 1, pp. 45–59, 2009.

[20] J.-H. Kim and G. H. Paulino, "Simulation of crack propagation in functionally graded materials under mixed-mode and non-proportional loading," *International Journal of Mechanics and Materials in Design*, vol. 1, no. 1, pp. 63–94, 2004.

[21] A. Oral, J. Lambros, and G. Anlas, "Crack initiation in functionally graded materials under mixed mode loading: experiments and simulations," *Journal of Applied Mechanics*, vol. 75, no. 5, Article ID 051110, 2008.

[22] S. S. V. Kandula, J. Abanto-Bueno, J. Lambros, and P. H. Geubelle, "Cohesive modeling of quasi-static fracture in functionally graded materials," *Journal of Applied Mechanics*, vol. 73, no. 5, pp. 783–791, 2006.

[23] E. T. Ooi, S. Natarajan, C. Song, and F. Tin-Loi, "Crack propagation modelling in functionally graded materials using scaled boundary polygons," *International Journal of Fracture*, vol. 192, no. 1, pp. 87–105, 2015.

[24] A. Kredegh, A. Sedmak, A. Grbovic, N. Milosevic, and D. Danicic, "Numerical simulation of fatigue crack growth in friction stir welded T-joint made of Al 2024 T351 alloy," *Procedia Structural Integrity*, vol. 2, pp. 3065–3072, 2016.

[25] H. Bayesteh and S. Mohammadi, "XFEM fracture analysis of orthotropic functionally graded materials," *Composites Part B: Engineering*, vol. 44, no. 1, pp. 8–25, 2013.

[26] A. Portela, M. H. Aliabadi, and D. P. Rooke, "Dual boundary element incremental analysis of crack propagation," *Computers & Structures*, vol. 46, no. 2, pp. 237–247, 1993.

[27] Y. Mi and M. H. Aliabadi, "Three-dimensional crack growth simulation using BEM," *Computers & Structures*, vol. 52, no. 5, pp. 871–878, 1994.

[28] P. H. Wen, M. H. Aliabadi, and Y. W. Liu, "Meshless method for crack analysis in functionally graded materials with enriched radial base functions," *Computer Modelling in Engineering & Sciences*, vol. 30, no. 3, pp. 133–147, 2008.

[29] S. A. Silling, "Reformulation of elasticity theory for discontinuities and long-range forces," *Journal of the Mechanics and Physics of Solids*, vol. 48, no. 1, pp. 175–209, 2000.

[30] S. A. Silling and E. Askari, "A meshfree method based on the peridynamic model of solid mechanics," *Computers and Structures*, vol. 83, no. 17-18, pp. 1526–1535, 2005.

[31] F. Bobaru and G. Zhang, "Why do cracks branch? A peridynamic investigation of dynamic brittle fracture," *International Journal of Fracture*, vol. 196, no. 1-2, pp. 59–98, 2015.

[32] T. L. Warren, S. A. Silling, A. Askari, O. Weckner, M. A. Epton, and J. Xu, "A non-ordinary state-based peridynamic method to model solid material deformation and fracture," *International Journal of Solids and Structures*, vol. 46, no. 5, pp. 1186–1195, 2009.

[33] J. T. Foster, S. A. Silling, and W. W. Chen, "Viscoplasticity using peridynamics," *International Journal for Numerical Methods in Engineering*, vol. 81, no. 10, pp. 1242–1258, 2009.

[34] R. W. Macek and S. A. Silling, "Peridynamics via finite element analysis," *Finite Elements in Analysis and Design*, vol. 43, no. 15, pp. 1169–1178, 2007.

[35] U. Yolum, A. Taştan, and M. A. Güler, "A peridynamic model for ductile fracture of moderately thick plates," *Procedia Structural Integrity*, vol. 2, pp. 3713–3720, 2016.

[36] E. Oterkus, I. Guven, and E. Madenci, "Fatigue failure model with peridynamic theory," in *Proceedings of the IEEE Intersociety Conference on Thermal and Thermomechanical Phenomena in Electronic Systems*, pp. 1–6, Las Vegas, NV, USA, June 2010.

[37] S. A. Silling and A. Askari, "Peridynamic model for fatigue cracking," Technical Report no. SAND2014-18590, Sandia National Laboratories, Albuquerque, NM, USA, 2014.

[38] G. Zhang, Q. Le, A. Loghin, A. Subramaniyan, and F. Bobaru, "Validation of a peridynamic model for fatigue cracking," *Engineering Fracture Mechanics*, vol. 162, pp. 76–94, 2016.

[39] J. Jung and J. Seok, "Fatigue crack growth analysis in layered heterogeneous material systems using peridynamic approach," *Composite Structures*, vol. 152, pp. 403–407, 2016.

[40] J. Jung and J. Seok, "Mixed-mode fatigue crack growth analysis using peridynamic approach," *International Journal of Fatigue*, vol. 103, pp. 591–603, 2017.

[41] Y. L. Hu and E. Madenci, "Peridynamics for fatigue life and residual strength prediction of composite laminates," *Composite Structures*, vol. 160, pp. 169–184, 2017.

[42] E. Madenci and E. Oterkus, *Peridynamic Theory and its Applications*, Springer, New York, NY, USA, 2014.

[43] F. Bobaru, H. G. Philippe, A. S. Stewart, and J. T. Forster, *Handbook of Peridynamic Modeling*, CRC Press, Boca Raton, FL, USA, 2016.

[44] B. Kilic and E. Madenci, "An adaptive dynamic relaxation method for quasi-static simulations suing the peridynamic theory," *Theoretical and Applied Fracture Mechanics*, vol. 53, no. 3, pp. 194–204, 2010.

[45] Q. V. Le, W. K. Chan, and J. Schwartz, "A two-dimensional ordinary, state-based peridynamic model for linearly elastic solids," *International Journal for Numerical Methods in Engineering*, vol. 98, no. 8, pp. 547–561, 2014.

[46] D. Huang, G. Lu, and P. Qiao, "An improved peridynamic approach for quasi-static elastic deformation and brittle fracture analysis," *International Journal of Mechanical Sciences*, vol. 94-95, pp. 111–122, 2015.

[47] Q. V. Le and F. Bobaru, "Surface corrections for peridynamic models in elasticity and fracture," *Computational Mechanics*, vol. 61, no. 4, pp. 499–518, 2018.

[48] American Society for Testing Materials (ASTM), *Standard Test Method for Measurement of Fatigue Crack Growth Rates*

(E647-11), American Society for Testing Materials (ASTM), West Conshohocken, PA, USA, 2011.

[49] A. Tzamtzis, *Fatigue crack growth prediction under mode I loading in friction stir aluminum alloy weld*, Ph.D. thesis, Dept. of Mechanical Engineering, University of Thessaly, Thessaly, Greece, 2015.

[50] F. Wang, Y. E. Ma, Y. N. Guo, and W. Huang, "Numerical studies on mixed-mode crack propagation behavior for functionally graded material based on peridynamic theory," *International Journal of Computational Materials Science and Engineering*, vol. 7, no. 4, Article ID 1850027, 2018.

[51] Y. E. Ma, P. Staron, T. Fischer, and P. E. Irving, "Size effects on residual stress and fatigue crack growth in friction stir welded 2195-T8 aluminium-part II: modelling," *International Journal of Fatigue*, vol. 33, no. 11, pp. 1426–1434, 2011.

[52] Y. D. Ha and F. Bobaru, "Studies of dynamic crack propagation and crack branching with peridynamics," *International Journal of Fracture*, vol. 162, no. 1-2, pp. 229–244, 2010.